Iceland rising: Solid Earth response to ice retreat inferred from satellite radar interferometry and visocelastic modeling

A. Auriac,[1] K. H. Spaans,[1] F. Sigmundsson,[1] A. Hooper,[2] P. Schmidt,[3] and B. Lund[3]

Received 3 July 2012; revised 22 December 2012; accepted 3 January 2013; published 8 April 2013.

[1] A broad uplift occurs in Iceland in response to the retreat of ice caps, which began circa 1890. Until now, this deformation signal has been measured primarily using GPS at points some distance away from the ice caps. Here, for the first time we use satellite radar interferometry (interferometric synthetic aperture radar) to constrain uplift of the ground all the way up to the edge of the largest ice cap, Vatnajökull. This allows for improved constraints on the Earth rheology, both the thickness of the uppermost Earth layer that responds only in an elastic manner and the viscosity below it. The interferometric synthetic aperture radar velocities indicate a maximum displacement rate of 24±4 and 31±4 mm/yr at the edge of Vatnajökull, during 1995–2002 and 2004–2009, respectively. The fastest rates occur at outlet glaciers of low elevation where ice retreat is high. We compare the observations with glacial isostatic adjustment models that include the deglaciation history of the Icelandic ice caps since 1890 and two Earth layers. Using a Bayesian approach, we derived probability density functions for the average Earth model parameters for three satellite tracks. Based on our assumptions, the three best fit models give elastic thicknesses in the range of 15–40 km, and viscosities ranging from 4–10× 10^{18} Pa s.

Citation: Auriac, A., K. H. Spaans, F. Sigmundsson, A. Hooper, P. Schmidt, and B. Lund (2013), Iceland rising: Solid Earth response to ice retreat inferred from satellite radar interferometry and visocelastic modeling, *J. Geophys. Res. Solid Earth*, *118*, 1331–1344, doi:10.1002/jgrb.50082.

1. Introduction

[2] Ice caps cover about 11% of Iceland [*Björnsson*, 1978]. The largest of them is the Vatnajökull ice cap in the southeast of the country, which is about 90–115 km wide and 400 m thick on average (Figure 1). Vatnajökull has been retreating since ~1890, corresponding to the end of the Little Ice Age (LIA) in Iceland, as revealed by observations of terminus positions of outlet glaciers and mass balance studies [e.g., *Björnsson*, 1978; *Björnsson et al*., 2002; *Björnsson and Pálsson*, 2008]. This ice retreat induces a ground uplift of more than 20 mm/yr [e.g., *Pagli et al*., 2007; *Árnadóttir et al*., 2009]. The Vatnajökull ice cap covers several volcanic systems, each consisting typically of a central volcano and an associated fissure swarm (Figure 1). The volcanic systems are part of the plate boundary between the North American and Eurasian plates, which is complex in Iceland due to the interaction between the mid-oceanic ridge and a mantle plume centered beneath northwestern Vatnajökull. Recent studies [e.g., *Pagli and Sigmundsson*, 2008; *Albino et al*. 2010; *Sigmundsson et al*. 1919; *Hooper et al*. 2011] showed that the ongoing uplift is affecting magmatism and melt production under Iceland.

[3] The rheology of the crust and mantle in Iceland has been inferred from ice mass changes at Icelandic ice caps from studies considering different temporal and spatial scales: (i) the postglacial response due to the melting of the ice cap that entirely covered Iceland during the last glacial maximum, and (ii) the present-day ongoing retreat of the Icelandic ice caps since the end of the LIA. Geologic data, such as dated uplifted marine deposits, from the end of the Weichselian glaciation approximately 10,000 years ago [e.g., *Norðahl et al*. 2008], form the basis for the first approach. Models for uplift after the disappearance of the Weichselian ice cap in Iceland, which appears to have been completed in about 1000 years, suggest a maximum viscosity under Iceland of 10^{19} Pa s [*Sigmundsson*, 1991], much lower than in Fennoscandia, for example. In the second case, addressed here, studies deal with countrywide uplift with maximum around present-day ice caps, which is dominated by the last ~120 years of ice retreat. Present-day deformation around Vatnajökull ice cap has been mapped previously by various geodetic techniques, including GPS, gravimetry, and tilt measurements (see references in Table 1). The maximum observed deformation was 23 mm/yr (Table 1). These data have been used to infer Earth rheology, most frequently in the form of an uppermost elastic layer underlain by a viscoelastic material. Results indicate an elastic layer of 5–40 km thickness and viscosities on the order of 10^{18}–10^{19} Pa s (Table 1). Furthermore, annual cycles in the Earth deformation, caused by seasonal variations in snow and ice load, have been studied with continuous GPS [e.g., *Grapenthin et al*., 2006]. A maximum annual peak-to-trough vertical displacement of ~37 mm is predicted under

[1]Nordic Volcanological Center, Institute of Earth Sciences, University of Iceland, Reykjavík, Iceland.
[2]Department Geoscience and Remote Sensing, Delft University of Technology, Delft, The Netherlands.
[3]Department of Earth Sciences, Uppsala University, Uppsala, Sweden.

Corresponding author: A. Auriac, Nordic Volcanological Center, Institute of Earth Sciences, University of Iceland, Sturlugata 7, Reykjavík 101, Iceland. (ama3@hi.is)

2169-9313/13/10.1002/jgrb.50082

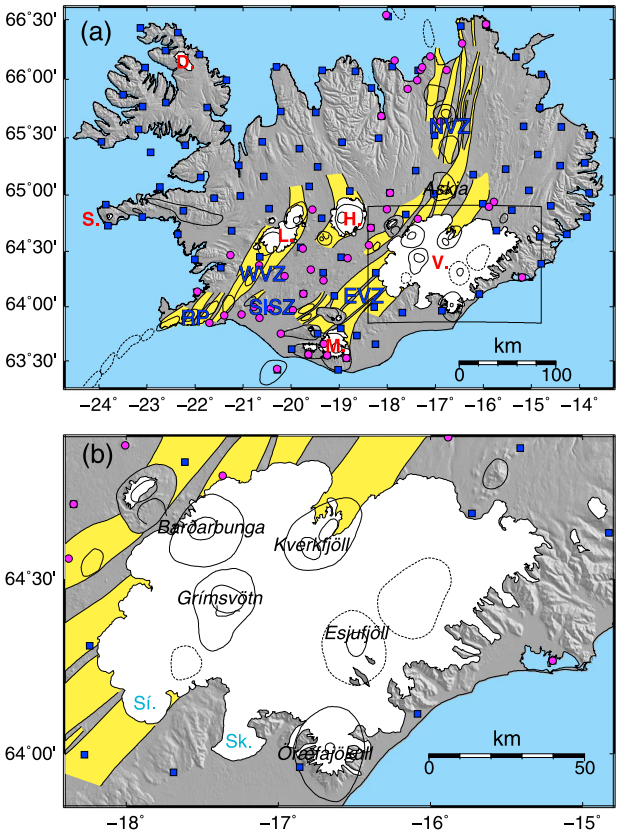

Figure 1. (a) Ice caps and tectonic setting of Iceland. Fissure swarms are shown in yellow and central volcanoes with their associated calderas (after *Einarsson and Saemundsson* [1987]) are represented by oval outlines. Names of the plate boundary segments are indicated in blue (NVZ: Northern Volcanic Zone, EVZ: Eastern Volcanic Zone, WVZ: Western Volcanic Zone, SISZ: South Iceland Seismic Zone, and RP: Reykjanes Peninsula). Main ice cap names are indicated in red (D.: Drangajökull, S.: Snæfellsjökull, L.: Langjökull, M.: Mýrdalsjökull, H.: Hofsjökull, and V.: Vatnajökull). (b) Zoom of the Vatnajökull ice cap. Names in light blue correspond to the outlet glaciers discussed in this study (Sí.: Síðujökull, Sk.: Skeiðarárjökull). For Figures 1a and 1b, names in italic indicate key volcanoes, blue squares show the location of the GPS stations used for the ERS period, and the purple circles the GPS stations used for the Envisat period.

Vatnajökull and about 16 mm is observed at GPS stations closer to its margins.

[4] The aim of this study is to better constrain the ground uplift around Vatnajökull ice cap. It is a complex deformation signal composed of the short-term elastic response and long-term viscoelastic adjustment, caused by the general retreat of the ice cap over the past 120 years, and seasonal changes in snow and ice cover. We refer here to all these processes as glacial isostatic adjustment (GIA) as the signals we evaluate in this paper are dominated by the viscoelastic response to long-term ice retreat.

[5] In this study, we supplement GPS data with satellite radar interferometry (interferometric synthetic aperture radar, InSAR), which provides high spatial resolution. The first radar data were acquired in 1992 and the number of images available is high enough to allow accurate velocity estimates for deformation around Vatnajökull ice cap. The ongoing retreat of the ice caps, the relatively low viscosity beneath Iceland and the thin elastic lithosphere account for a short-wavelength GIA-induced signal in Iceland [e.g., *Árnadóttir et al.* 2009]. Therefore, it is easier to map and study GIA deformation in Iceland with the InSAR technique compared to most parts of the world. A total of almost 70 radar images were analyzed, covering the period from 1992–2002 over the southwest part of the ice cap and surroundings, and 2004–2009 to its east. They provide a detailed map of the displacement pattern and its lateral extent in those regions. Extensive snow cover is present in Iceland during the winter months, which decorrelates the radar measurements. Therefore, we selected only the images acquired between May and October. The effect of the annual cycles was therefore significantly reduced, and not explicitly estimated in this study. We used the data to constrain the rheology of the Earth in the southeastern part of Iceland. This was achieved by evaluating 90 parametrizations of a horizontally layered Earth model, where the viscoelastic field equations were solved by a finite element model, considering the geometry of Icelandic ice caps and spatially varying thinning rates of Vatnajökull.

2. Data and Analysis

2.1. InSAR Data

[6] InSAR requires at least two satellite acquisitions to create one (or more) interferogram(s), by comparing the microwave signal of each acquisition, which is transmitted from a satellite and scattered back to it from the Earth's surface. The advantage of this method, compared for example to GPS, lies in its superior spatial resolution and the fact that no field work is required. Each satellite scene has a width of approximately 100 km (for the satellite data used in this study), making it possible to obtain surface deformation signals over large areas with dense sampling (up to 20 m for the satellites used in this study). InSAR can resolve deformation only in the line of sight (LOS) direction between the satellite and the ground. Because the signal is transmitted at an angle from the vertical, the deformation signal is composed of both vertical and horizontal components. The scalar LOS displacement for any given point, d_{LOS}, can be expressed as

$$d_{\mathrm{LOS}} = \begin{bmatrix} u_{\mathrm{E}} & u_{\mathrm{N}} & u_{\mathrm{U}} \end{bmatrix} \begin{bmatrix} d_{\mathrm{E}} \\ d_{\mathrm{N}} \\ d_{\mathrm{U}} \end{bmatrix} \tag{1}$$

where u_{E}, u_{N}, and u_{U} are the east, north, and up components of the unit LOS vector, respectively, and d_{E}, d_{N}, and d_{U} are the east, north, and up components of the displacement vector, respectively. In our case, u_{E}, u_{N}, and u_{U} correspond approximately to ± 0.35, ± 0.10, and $+0.90$, respectively. The sign of u_{E} and u_{N} varies depending on the satellite track, which can be ascending (satellite flying approximately from south to north) or descending (approximately from north to south) (Table 2). The incidence angle (angle between the viewing direction to the satellite and the vertical) is relatively small for our data set ($\sim 20^\circ$ to $\sim 27^\circ$ from the near to the far range of the scene). Moreover, the signal we want to study is mostly dominated by vertical deformation, thus, the contribution of the horizontal component of the LOS

Table 1. Overview of Earth Model Parameters Inferred From Previous GIA Studies at Vatnajökull Ice Cap, Compared to This Study

Data / Acquisition Year	Max. Deformation Observed	Elastic Thickness [km]	Viscosity [Pa s]	Source
lake tilt 1959, 1991	0.26±0.06 μrad/yr away from ice cap	5–25	$1–50\times10^{18}$	*Sigmundsson and Einarsson* [1992]
–	~8 mm/yr	10	5×10^{18}	*Wolf et al.* [1997]
GPS 1992, 1996, 1999	17±4 mm/yr	10–20	$\geq5\times10^{17}$	*Sjöberg et al.* [2004]
GPS 1996, 2004	20±2–4 mm/yr	10–20	$4–10\times10^{18}$	*Pagli et al.* [2007]
GPS 1991, 1992, 1996, 1999	–	20–30	$1–2\times10^{18}$	*Fleming et al.* [2007]
GPS 1993, 2004	23 mm/yr	40	10×10^{18}	*Árnadóttir et al.* [2009][a]
GPS 1993, 2004	23 mm/yr	10	1×10^{20} and 10×10^{18}	*Árnadóttir et al.* [2009][b]
Gravity 1991–1999	–2±1 μGal/yr[c]	6 / 35[d]	$5\pm3\times10^{17}$ / 10^{19}[e]	*Jacoby et al.* [2009]
Temperature distribution and olivine rheological behavior	–	27–40	$2\times10^{18}-10^{19}$	*Barnhoorn et al.* [2011][f]
InSAR, GPS 1992–2002, 2004–2009	24–31±4 mm/yr	$20.9^{+4}_{-4.3}$ $32.8^{+6.9}_{-8.1}$ $20.3^{+8.6}_{-4.7}$	$9.35^{+0.95}_{-0.8}\times10^{18}$ $9.15^{+1.05}_{-1.2}\times10^{18}$ $5.15^{+1.1}_{-1}\times10^{18}$	This study[g]

[a]Best fit model with two Earth layers.
[b]Best fit model with three Earth layers. The first viscosity corresponds to a 30 km thick layer and the second to the half-space underneath.
[c]Relative to Höfn base station, and corresponding to ~20 mm/yr uplift at the ice margins.
[d]6 km on top of a mantle plume, 35 km around.
[e]The first value corresponds to the viscosity of the mantle plume solved for, the second one corresponds to the viscosity of the surroundings, assumed at the beginning.
[f]The Earth model parameters they found are not constrained by GIA as they did not tried to fit their model to any observation of the GIA process.
[g]The first, second, and third values of the elastic thickness and viscosities correspond to the best fit models found for ERS track 9, ERS track 238, and Envisat track 230, respectively.

displacement remains small compared to the vertical. It must also be noted that the signal observed in an interferogram represents displacement relative to a reference area chosen within the scene.

[7] For this study, we used ~70 acquisitions from the ERS-1, ERS-2, and Envisat missions. We selected three tracks: ERS track 9 and 238 covering the southwestern area of Vatnajökull, spanning 1993–2002 and 1992–2000, respectively, and Envisat track 230 covering the eastern half of the ice cap and spanning 2004–2009 (Table 2). Track 9 partly covers the plate boundary deformation zone of the Eastern Volcanic Zone (Figure 1) and overlaps with track 238.

2.2. InSAR Analysis

[8] We compressed the raw SAR data in the direction along the flight path of the satellite (azimuth direction) and perpendicular to it (range direction) in a process known as focusing. This was achieved using the Repeat Orbit Interferometry PACkage [*Rosen et al*. 2004]. The Delft Object-oriented Radar Interferometric Software [*Kampes and Usai*, 1999] was used to coregister the slave image to the master to estimate their offsets, and resample the slave pixels to the master pixel positions. We also used the Delft Object-oriented Radar Interferometric Software to remove the topographic phase using an Advanced Spaceborne Thermal Emission and Reflection Radiometer (ASTER) Digital Elevation Model - version 1, June 2009, which has a resolution of 1 arc-second (corresponding to 30 m in north-south direction and 13 m in east-west direction for the study area). To limit the issue of decorrelation, caused by long temporal and/or perpendicular baselines [*Zebker and Villasenor*, 1992], we used the Standard Method for Persistent Scatterers (StaMPS) developed by *Hooper et al*. [2007]. StaMPS identifies the persistent scatterers (PS) of a scene, i.e., the pixels for which the coherent sum is dominated by a strong scatterer. The StaMPS software also includes a three-dimensional phase unwrapping technique, utilizing the information in the time domain to aid the spatial unwrapping [*Hooper*, 2010]. For computing purposes, we reduced the data to a manageable size by resampling the identified PS to an 800 m grid. Finally, we removed the PS points located on the ice cap, because their deformation signal is contaminated by glacial movements (Table 2).

[9] We present here two outputs from the processing: a time series of unwrapped interferograms (providing cumulative displacement over time of the InSAR scene), and LOS velocities (linear velocities for every PS point estimated from the time series). The interferograms in the time series are affected by a spatially correlated source of error, caused by a spatially- and temporally-variable atmospheric phase delay and orbital errors affecting every SAR acquisition. The influence of these atmospheric errors on our LOS velocity estimates is much reduced, because they are typically not strongly correlated in time, and thus largely cancel during the velocity estimation, but we include any remaining atmospheric error in our stochastic model (see section 3.2).

2.3. GPS Data and Processing

[10] We used vertical components of published velocity estimates from GPS stations in Iceland (Figure 1). The horizontal components were not used because they are significantly affected by plate spreading. For the ERS period, the

Table 2. Overview of Satellite Data Used in This Study

Satellites	Track (A/D)[a]	Master	Perp. Baseline [m][b]	Time Span	# PS	# Resampled PS[c]
ERS-1 / ERS-2	9 (D)	19960917	–600.7–505.7	1993–2002	154,789	4096
	238 (D)	19980730	–561.5–722	1992–2000	391,895	4355
Envisat	230 (A)	20080611	–435.1–555	2004–2009	404,734	851[d]

[a]A and D stands for ascending and descending tracks, respectively.
[b]Minimum and maximum perpendicular baseline (distance between the satellites) between the acquisitions.
[c]Resampled number of PS, accounting for both the resampling of the original data set and the removal of the points on Vatnajökull ice cap.
[d]After resampling and removal of the northern part of the scene.

GPS velocity estimates were obtained from countrywide GPS observations spanning 1993–2004 [*Árnadóttir et al.* 2009]. A total of 100 GPS stations were left to use after rejection of stations from the original data set reported to be affected by other processes than GIA by *Árnadóttir et al.* [2009]. The vertical velocities range from –1.2 to 17.6 mm/yr with uncertainties of 0.6–1.7 mm/yr. For the Envisat period, we used velocites for 2004–2009 estimated from continuous GPS measurements [*Geirsson et al.*, 2010; Geirsson, personal communication, 2012]. We used 43 of their vertical velocity estimates, again after excluding stations with vertical signal influenced by processes other than the GIA. GPS stations installed after 2008 or otherwise with insufficient data to provide reliable time series were also excluded. The velocities range from –1.1 to 25.0 mm/yr with formal uncertainties of 0.05–1.5 mm/yr. These uncertainties are lower than for the 1993–2004 period, because continuous GPS gives more accurate velocity estimates than campaign GPS measurements.

2.4. InSAR Time Series and Velocity Plots

[11] The InSAR time series (Figure 2) shows the cumulative ground displacement of the scene as a function of time, relative to a reference area chosen by the user (indicated by a star in Figures 2, 3, and 4). Although the deformation is calculated with respect to the master image (generally located in the middle of the stack of acquisitions), it is convenient to choose the earliest image as reference to display the results. Figure 2 shows an example of the 1993–2002 time series from track 9 of the ERS-1/2 satellites, mapping deformation around the southwestern edge of the Vatnajökull ice cap. A clear GIA-induced deformation signal is observed through time as progressive LOS shortening (in warm colors), in particular at Skeiðarárjökull outlet glacier. As explained in section 2.1, although some horizontal displacement also takes place, this LOS shortening is mostly due to vertical motion of the ground; GIA uplift in our case. The relative LOS shortening signal is up to 10–12 cm at the edge of the ice cap over the whole time period mapped. Also noticeable is the LOS lengthening at Síðujökull outlet glacier between October 1993 and May 1995. This signal is due to a glacial surge (a rapid destabilization and advance of a large mass of ice toward the glacier terminus), which occurred in 1994. The sudden displacement of ice toward the edge of the ice cap caused an elastic Earth response, resulting in the LOS lengthening pattern seen next to the ice in the interferograms that overlap in time with the surge [*Sigmundsson et al.*, 2006]. Surges at Icelandic outlet glaciers are a well known phenomenon and have occurred

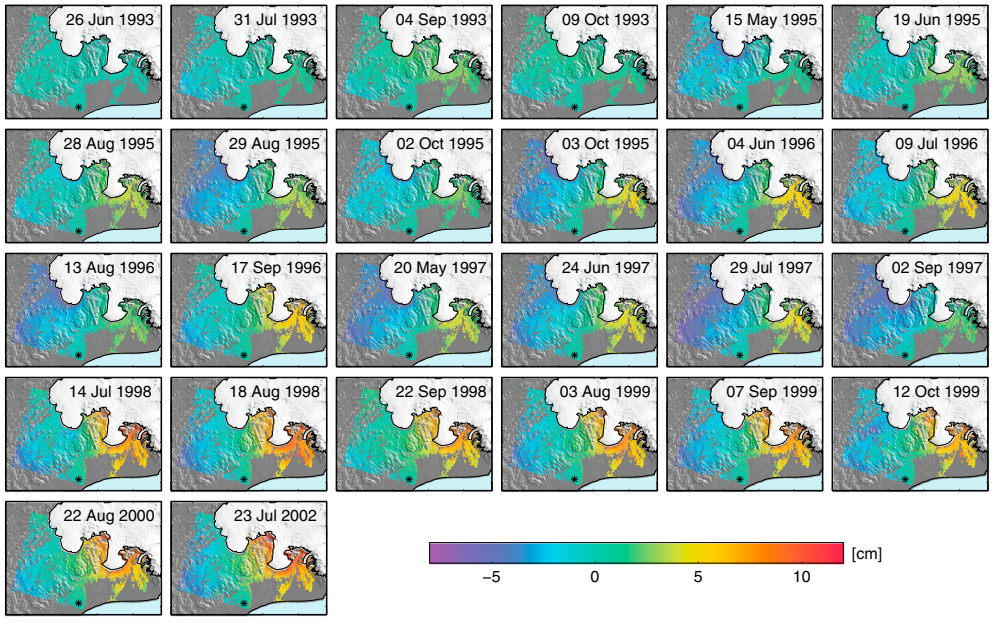

Figure 2. Time series of interferograms from ERS-1/2 satellites, track 9, spanning 1993 to 2002. Each interferogram shows the inferred cumulative relative LOS displacement from 26 June 1993 to time indicated in each panel. The star indicates the reference area.

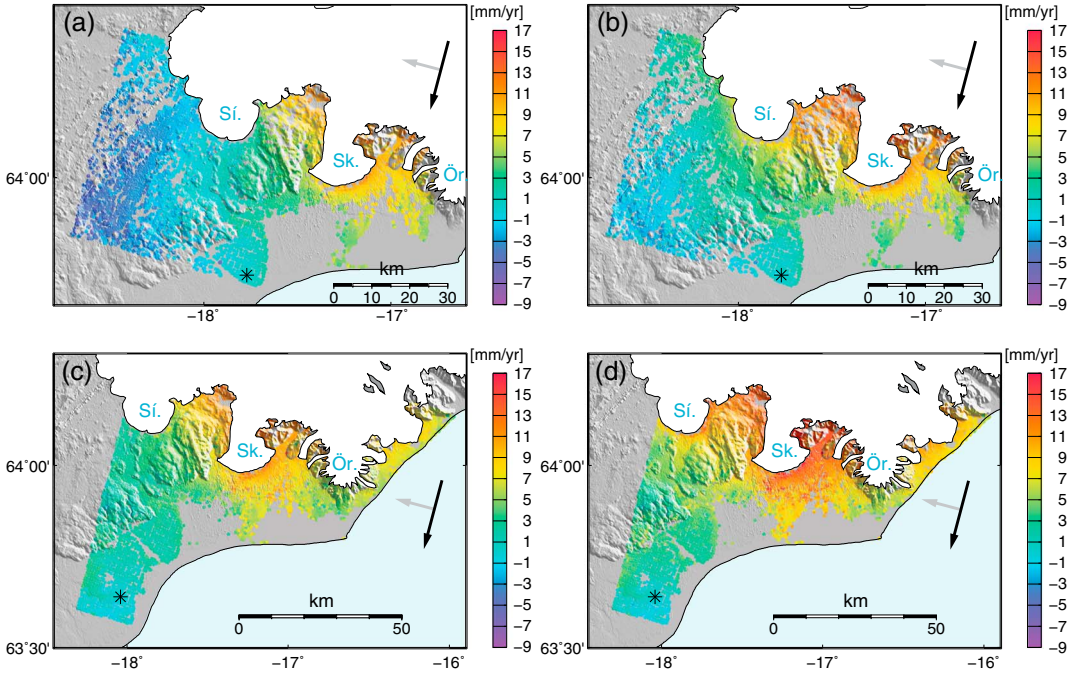

Figure 3. Inferred average LOS velocity from the two ERS-1/2 satellite tracks for the south and southwest of Vatnajökull: upper panels for track 9 and lower panels for track 238. LOS shortening is indicated in positive and warm colors. (a) and (c) Velocity plots calculated from all the interferograms, spanning 1993 to 2002 for track 9 and 1992 to 2000 for track 238; respectively. (b) and (d) Velocity plots where the effects from the surge of Síðujökull has been removed, by using only the interferograms after 1995. Names in light blue are key outlet glaciers (Sí.: Síðujökull, Sk.: Skeiðarárjökull, Ör.: Öræfajökull). The black and grey arrows show the azimuth of the satellite and the look direction, respectively; the star indicates the reference area.

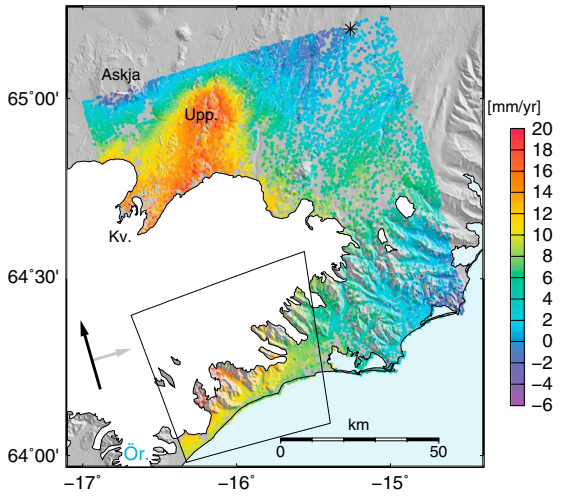

Figure 4. Inferred average LOS velocity from Envisat satellite, track 230, covering the east of Vatnajökull, spanning 2004 to 2009. LOS shortening is indicated in positive and warm colors. Names in black indicate key locations: Askja caldera, Upptyppingar intrusion (Upp.), and Kverkfjöll volcano (Kv.); the name in light blue is the key outlet glacier (Ör.: Öræfajökull). The black and grey arrows show the azimuth of the satellite and the look direction, respectively; the star indicates the reference area. The black box indicates the area containing the PS points used in the comparison between data and models.

many times in the last century [*Björnsson and Pálsson*, 2008]. The time series in Figure 2 also displays some variations in the signal in the western part of the scene (mostly between 1995–1997), which may indicate residual atmospheric effects or a contribution from the plate spreading. Some small variations can also be seen in the rest of the scene, which could also be explained by residual atmospheric signals or seasonal variations in the GIA signal.

[12] The StaMPS processing outputs also an average velocity estimate for each PS point in the LOS direction, obtained by estimating a linear velocity from the displacement time series. The velocity is also relative to the chosen reference area. Errors in the time series, mostly caused by atmospheric effects and orbital errors, are expected to largely cancel during the velocity estimation. Clear GIA-induced LOS shortening, at a maximum at the edge of Vatnajökull and decaying away from it, is revealed by the LOS velocity plots (Figures 3 and 4). Inferred LOS velocities in the overlapping area of the two ERS tracks show good consistency between the tracks, considering the different reference areas. The observations reveal a clear variation in LOS velocities along the edge of the ice cap, which appears to be an important feature of the GIA pattern. The difference in LOS velocity between the two neighboring outlet glaciers Skeiðarárjökull and Öræfajökull is ~10 mm/yr (Figure 3). We attribute this to a difference in ice retreat. Skeiðarárjökull is an outlet glacier reaching low altitude (~200–300 m above sea level) and experiences a fast retreat. In contrast, Öræfajökull is the highest elevation in Iceland (~2100 m)

and most of it is well above the glaciation limit of 1100 m for southern Iceland [*Björnsson and Pálsson*, 2008]. Skeiðarárjökull is retreating faster than Öræfajökull, leading to a greater response of the Earth at the former. North of Vatnajökull ice cap (Figure 4), a wide elongated pattern of LOS shortening is caused by a magmatic intrusion in the Mt. Upptyppingar area (see next paragraph). Apart from this, the observed pattern of LOS change caused by GIA over the eastern half of the study area is similar as in the south and west of the ice cap (seen on Figure 3). However, the maximum displacement rate recorded at the edge of the ice cap on the Envisat track gradually decreases by ~11 mm/yr from the southern ice edge to the easternmost part of the ice cap. This variation can be explained by less unloading occurring to the east [*Björnsson and Pálsson*, 2008] and because this area is further away from the center of ice loss, located more to the west.

[13] Additional signals, as seen on the LOS velocity plots, obscure the GIA-induced deformation pattern around the ice cap. The most noticeable signal is due to the large deformation east of the Askja caldera, in the region of Mt. Upptyppingar (Figure 4). The signal was caused by a lower crustal dike intrusion, which took place from February 2007 to April 2008, as discussed by *Hooper et al*. [2011]. They showed that the geometry of the dike may have been influenced by the stress field induced by the GIA process. Because of the proximity of the dike intrusion to the Vatnajökull ice cap, the GIA and the dike signals merge to form an elongated pattern. One can also observe a LOS shortening signal east of the ice cap, the origin of which remains unclear at this moment. Another additional signal is observed near the upper left corner of this track. LOS lengthening there is due to ongoing deflation of Askja caldera, located just outside of the scene [e.g., *Sturkell et al*. 2006; *de Zeeuw-van Dalfsen et al*. 2012]. Comparison of velocities in the left and right panels in Figure 3 reveal the importance of the 1994 surge at Síðujökull outlet glacier on the GIA pattern. Including the images that span the time of the surge when calculating the average LOS velocity lowers the uplift estimate around this outlet glacier by ~8 mm/yr. In this case, the subsidence signal caused by the surge obscures the GIA signal, leaving a relative subsidence pattern on the left panels of Figure 3 compared to the relative uplift seen on the right panels of the same figure.

[14] The additional signals influence the velocity fields significantly and may cause some bias when comparing the InSAR LOS velocity to the modeling results. To compensate for the surge signal around the Síðujökull outlet glacier (Figure 3), we decided to only use the InSAR data acquired in 1995 and later. This enabled us to remove most of the induced signal from the surge caused by the rapid elastic response of the Earth. Some viscoelastic deformation due to the surge will still occur after 1995, but it will be less significant than the elastic response and will only produce a small perturbation in the GIA signal. This is confirmed by the time series of ERS tracks 9 and 238 starting in 1995, which do not show any clear evidence of a viscoelastic response to the surge. The signals around the Askja caldera, the Upptyppingar region, and the LOS shortening east of the ice cap (Figure 4) cannot be removed by excluding radar images. The subsidence of Askja volcano is an ongoing process and therefore influences all the satellite acquisitions. The signal to the east also seems to be present throughout the whole time period. Due to the timing of the Upptyppingar intrusion compared to the time spanned by our data, removing the acquisitions from the intrusion would leave too few acquisitions to estimate a reliable velocity. For this track, because of all the signals present in the scene that are not caused by GIA, we used only the PS points south of Vatnajökull when comparing the observations to the models (Figure 4).

3. Modeling

[15] Modeling of the GIA deformation was carried out with the commercial finite element software Abaqus, following the same methodology as *Wu* [2004] and *Árnadóttir et al*. [2009]. We assumed a flat isotropic Earth. Models were built as a box of $2000 \times 2000 \times 1000$ km in the east-west, north-south, and depth directions, respectively. A series of tests were carried out to infer that this was the minimum size of the box for which boundary conditions did not have a significant influence on the displacement. Each box was then divided into two horizontal layers: an elastic layer on top of a viscoelastic layer. A Poisson's ratio of 0.25 and Young's modulus of 90×10^9 Pa (as used by *Pagli et al*. [2007]) were assumed for both layers. We decided to vary only two of the parameters used in the modeling to infer the best-fit values: (i) the thickness of the elastic layer, varied from 5 to 60 km (5 km step size in the 0–30 km depth range and 10 km below), and (ii) the viscosity of the lower layer, with viscosities ranging from $2–20 \times 10^{18}$ Pa s (step size of 2×10^{18} Pa s), similar to *Árnadóttir et al*. [2009]. Buoyancy effects were included at every density discontinuity (free surface and interface between two layers) applying spring elements (with spring constant equals $\delta\rho \times g$ where $\delta\rho$ is the difference in density between the two materials at the interface, and g is the gravitational acceleration), as described by *Wu* [2004] and *Schmidt et al*. [2012b]. The density of the upper layer and the viscoelastic layer were set to 2800 kg/m^3 and 3200 kg/m^3, respectively. The load was then applied at the surface as distributed surface pressure, as explained in more detail in section 3.1. The outside boundaries of the model were pinned, allowing no displacement there. The meshing was achieved using tetrahedron elements with 3 degrees of freedom. The mesh is identical for the upper 5 km of all the models, denser at the center and decaying slowly with distance. In the load region of Vatnajökull, the space between nodes varies from ~265 m at the center to ~1137 m 50 km away, approximately at the ice edge, and the surface of the model consists of ~110,500 nodes.

3.1. Ice Model

[16] *Pagli et al*. [2007], *Fleming et al*. [2007], and *Árnadóttir et al*. [2009] have shown that the pre-1890 load history had little effect on the GIA modeling results, given the uncertainties on the observations. Thus, we decided to initialize the models at the end of the LIA in 1890. We assumed isostatic equilibrium in 1890 and used the ice history model developed by *Schmidt et al*. [2012a]. This model is based on an estimated ice loss of Vatnajökull of 435 km^3 between 1890–2004 [*Pagli et al*. 2007] linearly extrapolated to 458 km^3 up until 2010. Because the ice model was developed for quadratic elements and applied to our tetrahedron elements, the total ice loss over the past 120 years in our models is slightly different than that used by *Schmidt et al*.

[2012a]. The resulting volume of our implementation is about 453 km^3, giving a difference of ~1% between the two implementations. A spatially varying melting rate over Vatnajökull (Figure 5) was defined based on annual net mass balance estimates by *Björnsson and Pálsson* [2008]. In addition to Vatnajökull, the model includes other glaciers in Iceland (but not Drangajökull and Snæfellsjökull in the far northwest and west, respectively) for which a constant melting rate of 65 cm/yr was assumed. This corresponds to the average melting rate of the outer regions of Vatnajökull (Figure 5). This rate might not be exactly representative of the average melting rate at these glaciers but is sufficient for the scope of this study, because the area mapped by our InSAR data is located only around Vatnajökull ice cap. The ice model assumes a constant ice mass loss rate, over the 120 year period from 1890 to 2010. Our 90 GIA models were run for 120 years and outputs for the surface displacements were taken every 2 years. Velocity estimates covering the period spanned by our three InSAR sets of acquisitions were extracted from each model run. Finally, we ran three additional models corresponding to the three best-fit model for each InSAR track.

3.2. Model Fit and Parameter Probability Estimation

[17] To evaluate the range of model parameters compatible with the data, we followed a general statistical approach, similar to the one used by *Hooper et al*. [2012]. We estimated a probability distribution on the joint data sets for each track, using Bayes' rule (Appendix A). Assuming a multivariate Gaussian distribution for the measurement errors and a uniform prior probability for data and model, Bayes' rule can be written as

$$p(\mathbf{m}|\mathbf{d}) = K\frac{1}{\sqrt{(2\pi)^n|\mathbf{Q}|}}\exp\left[-\frac{WRSS}{2}\right] \tag{2}$$

where K is a constant, n is the number of observations, and $\mathbf{Q}$ is the variance-covariance matrix. $\mathbf{Q}$ is considered diagonal for the GPS data, because the inferred velocities are mostly independent. The InSAR measurements are on the other hand highly correlated in space. Accordingly, we estimated the full variance-covariance matrix for the InSAR observations (see method in Appendix B). $\mathbf{Q}$ then accounts for residual atmospheric, decorrelation, and unwrapping errors. The weighted residual sum of squares (WRSS) was calculated for each model, separately for the InSAR and GPS data sets, such that

$$WRSS = (\mathbf{d} - \mathbf{G}(\mathbf{m}))^{\mathrm{T}}\mathbf{Q}^{-1}(\mathbf{d} - \mathbf{G}(\mathbf{m})) \tag{3}$$

where $\mathbf{d}$ is the vector of the data (LOS velocity estimates for the InSAR and vertical velocity estimates for the GPS), $\mathbf{m}$ is the model vector, and $\mathbf{G}(.)$ is the model function that maps the model parameters to the observations. $\mathbf{G}(.)$ includes the GIA model, which gives east, north, and vertical displacements at a regular spacing, the linear interpolation of the model points to the observation points and conversion to LOS for InSAR observations. The residuals, given by $\mathbf{d} - \mathbf{G}(\mathbf{m})$, were calculated for each combination of model parameters. To estimate the residuals for model values in between those evaluated, we performed linear interpolation of the calculated residuals for the evaluated models. In the case of the InSAR, the LOS velocities are relative to a reference area; however, the models give absolute displacements, leading to a systematic offset between the two. Furthermore, although residual orbital signals are expected to largely cancel during the velocity estimation, some residual error, approximately resembling a bilinear ramp, will remain. We therefore used weighted least squares to estimate and subtract a plane from the residuals.

[18] To generalize our method for the probability distribution estimate, we included a scaling factor, σ^2, applied to the variance-covariance matrices of the InSAR and GPS data sets. It can account, for example, for model errors associated with the difference in spatial coverage between the two data sets. We might expect our simple model to fit less well close to the ice caps, leading to more model errors associated with the InSAR data set than with GPS. InSAR and GPS measurements are independent of each other so their contributions can be considered separately. Equations (2) and (3) can be rewritten, to include the scaling factors by substituting $\sigma_I^2\mathbf{Q_I}$ for $\mathbf{Q_I}$ and $\sigma_G^2\mathbf{Q_G}$ for $\mathbf{Q_G}$ (where subscripts I and G stand for InSAR and GPS, respectively). The posterior probability then becomes

$$p(\mathbf{m}|\mathbf{d}) = K\frac{\sigma_I^{-n_I}\times\sigma_G^{-n_G}}{\sqrt{(2\pi)^{n_G}|\mathbf{Q_G}|}\sqrt{(2\pi)^{n_I}|\mathbf{Q_I}|}} \tag{4}$$

$$\exp\left[-\frac{(\mathbf{d_G} - \mathbf{G_G}(\mathbf{m}))^{\mathrm{T}}\mathbf{Q_G}^{-1}(\mathbf{d_G} - \mathbf{G_G}(\mathbf{m}))}{2\sigma_G^2} - \frac{(\mathbf{d_I} - \mathbf{G_I}(\mathbf{m}))^{\mathrm{T}}\mathbf{Q_I}^{-1}(\mathbf{d_I} - \mathbf{G_I}(\mathbf{m}))}{2\sigma_I^2}\right]$$

σ_I^2 and σ_G^2 are constant for all combinations of model parameters and were calculated from our best WRSS estimate for each InSAR and GPS data sets individually such that

$$\frac{(\mathbf{d} - \mathbf{G}(\mathbf{m}))^{\mathrm{T}}\mathbf{Q}^{-1}(\mathbf{d} - \mathbf{G}(\mathbf{m}))}{\sigma^2} = n \tag{5}$$

where n is the number of observations used. From equation (4), we obtained the joint probability distribution of InSAR and GPS data for each of our three tracks separately. We set the constant term, K, such that the total probability equals one. We then determined our uncertainty region as the area that contains 95% of the total probability.

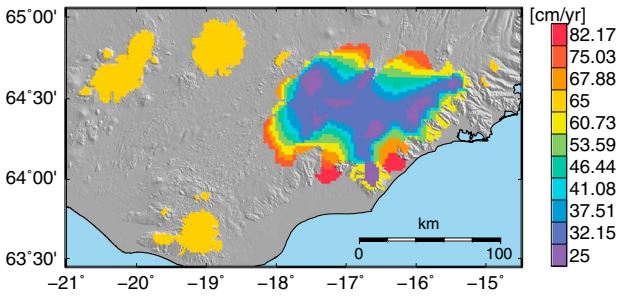

Figure 5. Thinning rates assumed in the ice model developed by *Schmidt et al*. [2012a]. For Vatnajökull, 10 regions with different melting rate were assumed, increasing from 25 cm/yr in the interior parts to up to 82.17 cm/yr at the ice-edge. For the other major ice caps, the thinning rate is constant at 65 cm/yr. Drangajökull and Snæfellsjökull ice caps are not taken into account in the modeling.

4. Results

[19] The results of the comparison between the data and the models are summarized in Figures 6 to 9. Figure 6 shows the WRSS estimated with the scaled GPS and InSAR data separately, and the combination of both, for each track. The WRSS for the GPS data resolves the viscosity well, but constrains the elastic thickness poorly. The scaled WRSS plot for the InSAR data shows a more complex pattern, spanning a wider range of viscosities and preferring in general a thinner elastic layer. This difference between the WRSS for the GPS and InSAR data can be explained by the fact that we remove bilinear ramps from the InSAR data. This means that the InSAR data do not constrain the absolute magnitude of the displacements nor the spatial gradient. Rather, they constrain quadratic and higher order variations in the spatial displacement, which are sensitive to different aspects of Earth rheology. These terms are more significant close to the ice cap and are therefore not well constrained by the GPS measurements. The scaling factors for the InSAR variance-covariance matrix we derive (according to equation (5)) equal 1.48, 0.95, and 0.83 for track 9, 238, and 230, respectively. For the GPS data, the scaling factors are equal to 1.6 and 368.83 for the ERS and the Envisat periods, respectively. Most of the scaling factors are close to 1, showing that the best-fit models approximately fit the data within the expected error. However, for the GPS data covering the Envisat period, the scaling is higher, indicating that the data cannot be fit within the very low formal errors of the continuous GPS data. Taken together these results suggest that the model errors are greater than the data errors for the continuous GPS, but less than those of the campaign GPS and InSAR. Because the WRSS for InSAR and GPS are sensitive to different aspects of the Earth structure, the combination of both gives an improved resolution for both Earth parameters. The approach described

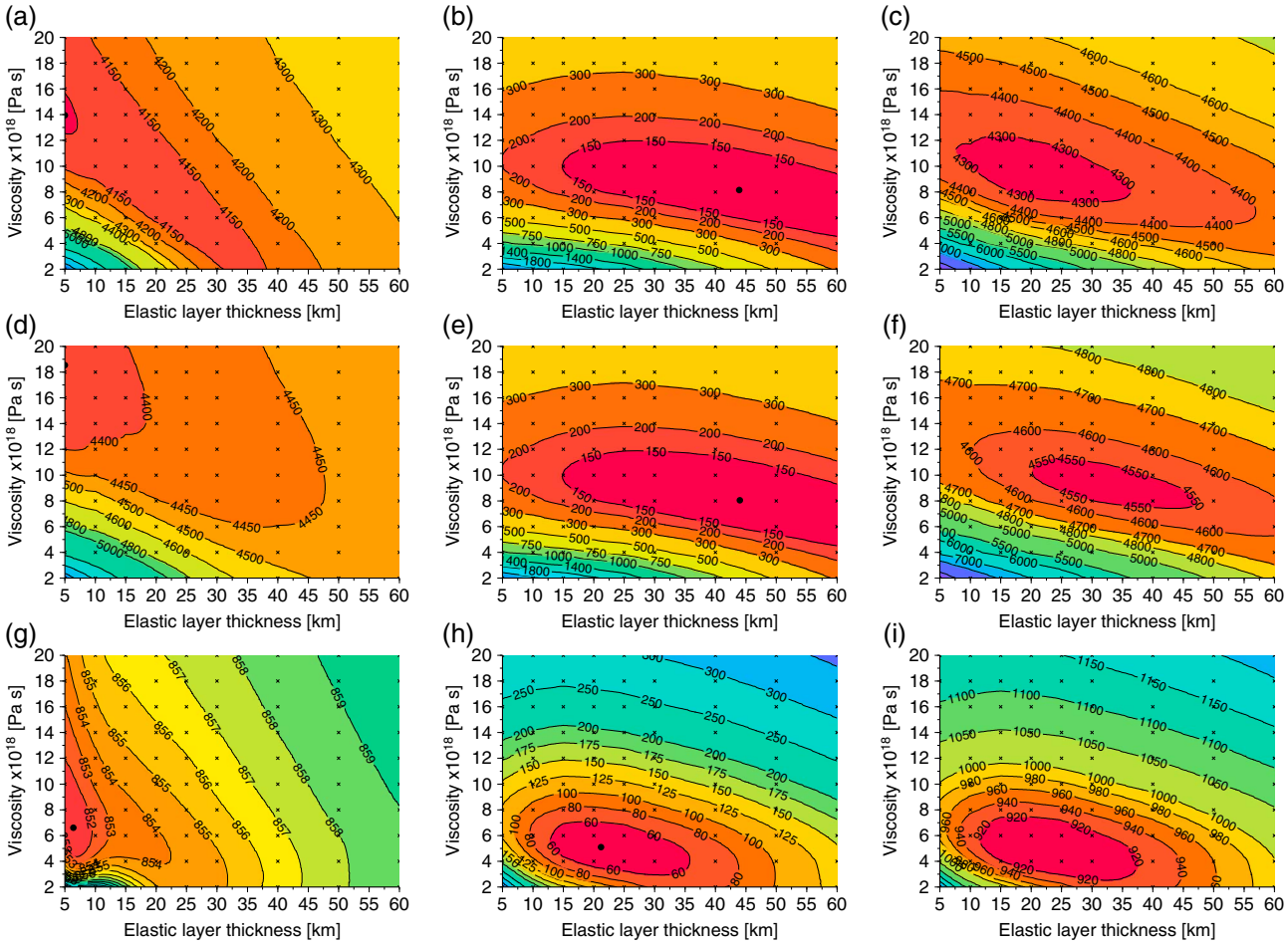

Figure 6. WRSS distributions for different data sets for models with thicknesses of elastic layer ranging from 5–60 km (x axis) and viscosities spanning 2–20$\times$ 10^{18} Pa s (y axis). (a), (b), and (c) The WRSS distribution for the InSAR data for ERS track 9, GPS data from the ERS time period and joint InSAR and GPS data sets, respectively. (d), (e), and (f) The InSAR data from ERS track 238 and the same time period for the GPS as above. (g), (h), and (i) The InSAR data from Envisat track 230 and the GPS data from the Envisat time period. The crosses represent the location of the models we ran and the black dots show the location of the lower WRSS for the InSAR and GPS data sets.

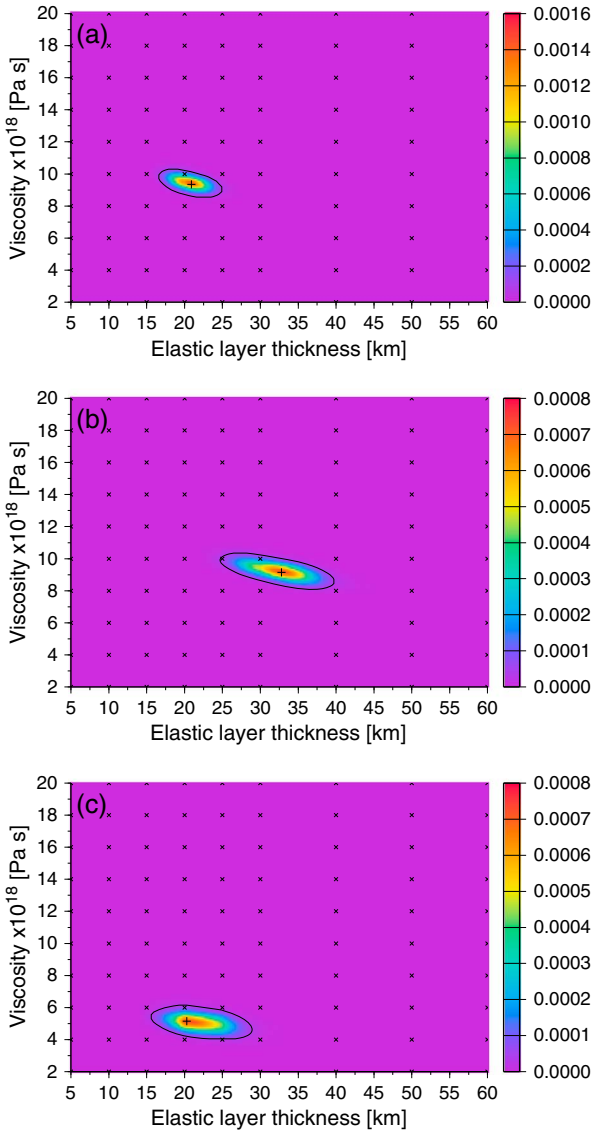

Figure 7. Joint InSAR and GPS probability distributions showing the best-fit Earth structure and the formal uncertainties defined by the 95% confidence region (black outline) for: (a) track 9, (b) track 238, and (c) track 230. Warm colors indicate the highest probabilities. The probabilities are normalized such that the area under the curve equals 1. The crosses represent the location of the models we ran and the pluses indicate the best-fit set of parameters for each track, corresponding to the best-fit model shown in Figure 8: (Figure 7a) elastic thickness of $20.9^{+4}_{-4.3}$ km and viscosity of $9.35^{+0.95}_{-0.8} \times 10^{18}$ Pa s, (Figure 7b) elastic thickness of $32.8^{+6.9}_{-8.1}$ km and viscosity of $9.15^{+1.05}_{-1.2} \times 10^{18}$ Pa s, and (Figure 7c) elastic thickness of $20.3^{+8.6}_{-4.7}$ km and viscosity of $5.15^{+1.1}_{-1} \times 10^{18}$ Pa s.

in the preceding section allows for the combination of the WRSS for GPS and InSAR into the joint probability distribution for each track, shown in Figure 7. This figure shows that the three tracks predict a different Earth structure beneath Vatnajökull. For the ERS tracks, the elastic layers barely overlap with $20.9^{+4}_{-4.3}$ km and $32.8^{+6.9}_{-8.1}$ km thickness, for tracks 9 and 238, respectively. The predicted viscosities are more similar with $9.35^{+0.95}_{-0.8} \times 10^{18}$ Pa s and $9.15^{+1.05}_{-1.2} \times 10^{18}$ Pa s for track 9 and 238, respectively. For the Envisat track 230, the best-fit model gives a $20.3^{+8.6}_{-4.7}$ km thick elastic layer associated with an underlying layer with a viscosity of $5.15^{+1.1}_{-1} \times 10^{18}$ Pa s. We consider these elastic thicknesses to be representative of the upper part of the Icelandic crust beneath Vatnajökull ice cap, which is estimated to be ~40 km thick in this region [*Darbyshire et al.* 1998].

[20] Figure 8 gives the InSAR LOS velocity, best-fit model and residual for the three tracks. The maximum LOS velocities, observed at the edges of the ice cap nearest to the center of mass of Vatnajökull, reach approximately 24 mm/yr for the two ERS tracks and 31 mm/yr for the Envisat track. The uncertainties on the InSAR velocities, estimated during the InSAR processing, reveal a standard deviation of 0.1–5.9 mm/yr for all the tracks, with 99% of the values falling in the 0.1–4 mm/yr range. The LOS velocities for the overlapping ERS tracks show some differences, especially when getting closer to the ice margin. This is clearly seen in Figures 8a and 8b and on the common profile shown in Figure 9. The difference between the two approximately resembles a bilinear ramp, and is due to the different best-fit models obtained for each data set.

[21] At the fastest retreating outlet glaciers, we observe that the best-fit model slightly underestimates the LOS velocity (Figures 8c and 8f). Local residual signal observed there reaches up to 6 mm/yr at Skeiðarárjökull and 4 mm/yr at Síðujökull. This is likely caused by an underestimation of the overall or more recent melting rate of those outlet glaciers, resulting in less modeled uplift than observed. The subsidence pattern around Askja caldera and uplift signals from the dike intrusion at Upptyppingar and to the east of the ice cap are visible on the residual plot from track 230 (Figure 8i), as they were not modeled.

5. Discussion

[22] Our InSAR observations, when corrected using the modeled bilinear ramp, show a maximum LOS change of 24±4 and 31±4 mm/yr at the edge of Vatnajökull ice cap, for the ERS and Envisat tracks, respectively. The method used provides a highly detailed set of data ranging from the ice edge to ~50–60 km away. The number of resampled PS within the area is more than 4000 for the ERS tracks and more than 800 for the southern part of the Envisat scene (Table 2). The high resolution of the InSAR observations enables us to resolve details in the GIA-induced uplift pattern, including high rates at the edge of the ice cap and variations in LOS velocities at neighboring glaciers, not accessed by previous studies. Uncertainties in InSAR observations are due to a combination of atmospheric artefacts, orbital effects, and unwrapping errors. The influence of atmospheric errors is greatly reduced in the estimated average LOS velocity and any remaining error is included in our stochastic model. Orbital uncertainties contribute to an error in the form of an approximately bilinear ramp, which we estimate deterministically. The three-dimensional unwrapping scheme in the StaMPS processing minimizes the probability of unwrapping errors. Any remaining unwrapping errors and decorrelation noise are also included in the stochastic model. The referenced InSAR velocities are also affected by the uncertainties in the best fit Earth model.

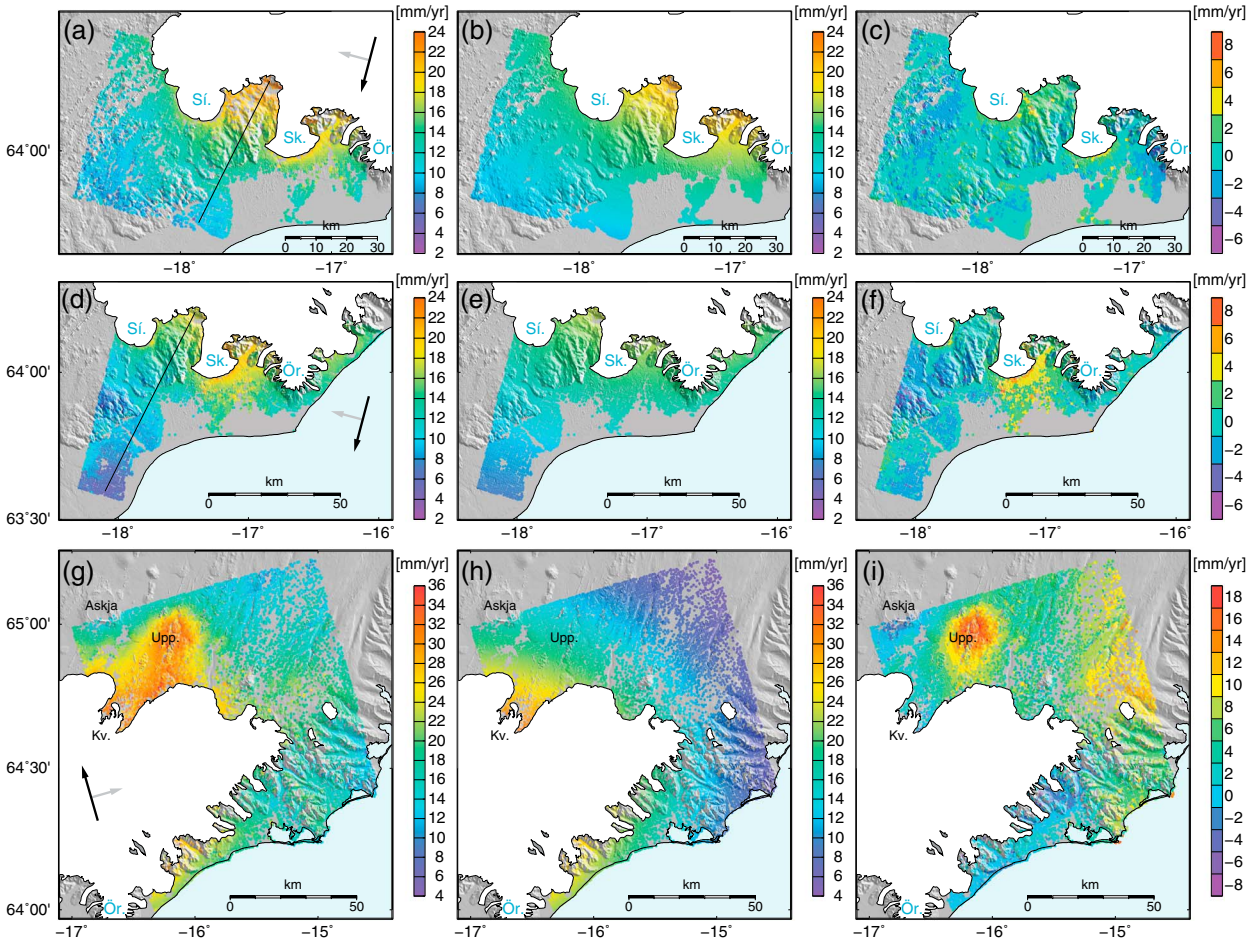

Figure 8. (a), (b), and (c) Referenced LOS velocity, best fit model converted to LOS and residuals between Figures 8a and 8b, respectively, for the ERS track 9 spanning 1995–2002. (d), (e), and (f) Same as above for the ERS track 238 spanning 1995–2000. The black line in Figures 8a and 8d indicates the profile from Figure 9. (g), (h), and (i) Same as above for the Envisat track 230 spanning 2004–2009. The referenced LOS velocities were obtained by compensating the relative InSAR velocities for the systematic offset between the model and the InSAR data as well as the orbital ramp estimated. On residual plots, warm colors indicate a model underestimation compared to the LOS velocity results. The black and grey arrows show the azimuth of the satellite and the look direction, respectively. Names in light blue are key outlet glaciers (Sí.: Síðujökull, Sk.: Skeiðarárjökull, Ör.: Öræfajökull). Names in black indicate key locations: Askja caldera, Upptyppingar intrusion (Upp.) and Kverkfjöll volcano (Kv.).

[23] Our LOS InSAR observations mostly reflect the vertical component of the displacement field. The LOS InSAR velocities can be directly compared to previous observations through equation (1). The time periods for a single set of our data (ERS or Envisat) are similar to the time covered in other studies. By comparing our observations to the literature, we find that our maximum LOS displacement rates are slightly higher than the results from GPS campaigns by *Sjöberg et al.* [2004], which indicate a maximum uplift of 17±4 mm/yr. Observations by *Pagli et al.* [2007] and *Árnadóttir et al.* [2009] reveal a maximum uplift rate of 20±(2–4) mm/yr and 23 mm/yr, respectively, also somewhat lower than our observations but within the uncertainties of our ERS estimates. The InSAR data set provides observations closer to the ice margin than in previous studies, so a difference in maximum uplift is to be expected. The Envisat LOS velocities are higher than the ERS values because the time period spanned is different and we expect more rapid uplift in recent years. The difference in the LOS InSAR velocities for the two ERS tracks indicates a high influence of the InSAR observations on the probability distributions and best fit models. Part of the area to the southwest of Vatnajökull is covered by both ERS tracks. However, track 9 also covers part of the eastern volcanic zone and track 238 shows the complete deformation around Öræfajökull. These two areas, not common to both tracks, are likely to play a significant role in the estimation of the best-fit model and therefore on the referenced LOS velocities. The difference between the probability distributions is also likely influenced by inaccuracies in the ice model. As the data go all the way to the ice cap and cover outlet glaciers with different uplift behaviors, it is likely that inaccuracies in the ice model will have a significant impact on the best fit model estimate.

[24] Our estimates for the model parameters and their uncertainty ranges depend on a number of model assumptions being true. We assumed a flat Earth and isotropic material

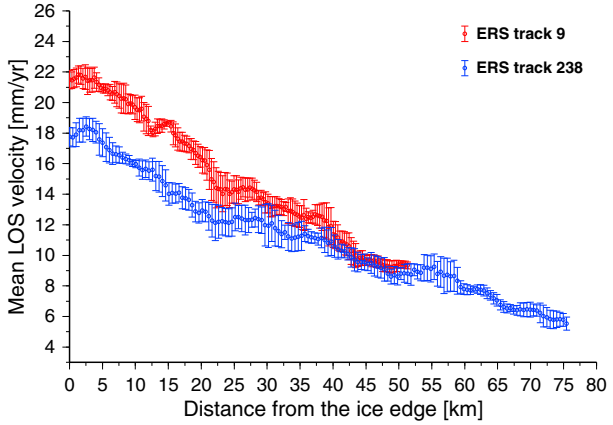

Figure 9. LOS velocity profiles from the ice edge toward the sea for ERS tracks 9 (in red) and 238 (in blue). The profile line for each track is shown in Figures 8a and 8d. A different ramp has been estimated and subtracted from each data set.

with horizontal layering. The flat Earth assumption is reasonable considering the size of Vatnajökull ice cap and the extent of the GIA signal, compared to studies over Fennoscandia, for example. The other assumptions are clearly a simplification of the real Earth, especially in our study area at a divergent plate boundary near the center of the hot spot, where we could expect lateral variations in the elastic thickness and viscosity. *Jacoby et al*. [2009] demonstrated the influence of lateral variations in the Earth's structure when comparing models to gravity data. However, they also showed that the results from these models do not provide a good fit to GPS data. The study by P. Schmidt et al. (Effects of present day deglaciation on melt production rates beneath Iceland, submitted to *Journal of Geophysical Research*, 2013) demonstrates that lateral variation in the elastic thickness results in up to 1.6 mm/yr difference in vertical displacement rate at the edge of the ice cap. *Schmidt et al*. [2012a] showed that, for the same GPS data used in this study for the ERS period, a homogeneous mantle fits the data as well as a model with layers of different viscosity. The assumed value of the Young's modulus (90 GPa) does influence the value of the derived model parameters. The value we have used corresponds to the higher end of values used in earlier studies (same as used by *Pagli et al*. [2007]). We also ran some models using a Young's modulus of 40 GPa, inferred to be the lower limit of the estimates for Iceland [*Grapenthin et al*., 2006]. While viscosity values are not significantly affected, elastic thickness values increase by ~15 km. This increase is larger than the range of our uncertainties for each individual probability density function, but within the overall range of elastic thickness for the different data sets. However, for the scope of this paper, this influence has not been considered any further.

[25] The ice model we use is detailed for Vatnajökull, but simpler for the other ice caps. They are outside our study area, however, and the use of a spatially averaged ice loss over the time period is presumed to be sufficient for comparison to our data. The ice model includes the assumption of a linear melting rate over the entire period, not taking into account seasonal variations or year-to-year fluctuations in the ice retreat due to climatic conditions. Such processes could have a significant effect on deformation in the short term, in particular through the elastic response of the Earth. Using a linear melting rate in our ice model assumes that these effects will average over time. Further studies should consider improvements to the spatial distribution of the ice model, especially at the fast retreating outlet glaciers where the residual plots point toward an underestimation of the ice loss. Higher LOS displacement rates in the Envisat period compared to ERS seem to indicate faster ice retreat after 2000. Our ice model uses constant melting rates and thus does not include the faster melting in the most recent years. This may also explain why the best model for the Envisat InSAR data predicts a lower viscosity than that predicted for the ERS data.

[26] The WRSS analyses for GPS and InSAR data separately give different constraints on the elastic thickness and viscosity. However, the combination of both provides a good resolution on both parameters, which can also be seen in the probability distribution plots. As well as depending on the model assumptions, our best fit models and 95% confidence regions also depend on the assumption that the measurement errors are multivariate Gaussian and well-estimated. As in all modeling studies, the 95% confidence region for the parameters is a formal uncertainty, which depends on the model assumptions being correct, and therefore represents a lower limit of the true uncertainty.

[27] Our estimates are influenced by the ongoing processes around Vatnajökull ice cap other than the GIA: (i) The plate boundary deformation zone is within and close to the scenes of our ERS tracks 9 and 238, respectively. Track 238 (Figure 8d) is mostly outside the boundary zone and no difference in the plate spreading velocities are expected within the scene (see GPS velocities by *Árnadóttir et al*. [2009]). Plate boundary deformation might influence our results, especially track 9, but there is no clear evidence of this. (ii) A glacial surge at Síðujökull outlet glacier in 1994 also creates some disturbance in the GIA signal. By removing the InSAR images spanning the surge, we removed most of the resulting signal from the surge, i.e., the elastic response. Some viscoelastic adjustment caused by the surge may still take place in years following the surge but we assume it to be negligible. (iii) The subsidence at Askja caldera and uplift pattern at Upptyppingar were also considered as a source of bias and were removed during the comparison between data and models, therefore not affecting our estimates.

[28] The best-fit models give elastic thicknesses of $20.9^{+4}_{-4.3}$ km, $32.8^{+6.9}_{-8.1}$ km, and $20.3^{+8.6}_{-4.7}$ km and viscosities of $9.35^{+0.95}_{-0.8} \times 10^{18}$ Pa s, $9.15^{+1.05}_{-1.2} \times 10^{18}$ Pa s, and $5.15^{+1.1}_{-1} \times 10^{18}$ Pa s for track 9, 238, and 230, respectively. The model parameters span the range of 15–40 km for elastic thickness and 4–10$\times 10^{18}$ Pa s for viscosity. These results are comparable or within the uncertainties of the values found in most previous studies based on GIA. In addition, *Barnhoorn et al*. [2011] also reached comparable results to ours, even though they did not use GIA observations to constrain their modeling but temperature distribution and olivine rheological behavior. Our viscosity estimates are 2–4 orders of magnitude lower than the normally inferred viscosities in tectonically stable regions where GIA is observed [e.g., *Peltier*, 2004; *Klemann and Wolf*, 2005; *Milne et al*., 2004; *Steffen and Kaufmann*, 2005]. In the subduction region of Alaska, *Larsen et al*. [2005] fitted their observations of glacial retreat,

however, with an asthenospheric viscosity of a 3.7×10^{18} Pa s. The main difference between regions like Alaska or Iceland and regions like Scandinavia or Greenland comes from their tectonic setting. In Iceland, there is the combination of a divergent plate boundary and a mantle plume, processes that increase the temperature of the lithosphere and asthenosphere, decreasing the viscosity and the elastic thickness. Moreover, it seems that the relatively thin elastic layer of typical divergent plate boundary settings (e.g., 8 to 10 km for the North Atlantic Ocean obtained by *Bowin and Milligan* [1985] and *Cochran* [1979], respectively) is not observed beneath Iceland, most likely because of the interaction with the mantle plume.

6. Conclusions

[29] InSAR has proven a successful and powerful additional tool in studying the ongoing GIA process in Iceland, revealing maximum LOS displacement rates of 24±4 and 31±4 mm/yr for the ERS and Envisat tracks, respectively, at the edge of Vatnajökull ice cap. The LOS shortening signal is clearly observed in our interferograms, with better spatial resolution than previously possible with GPS data alone. Uplift is resolved up to the ice edge, where the highest deformation rates are observed. We detect significant variation in LOS displacement rate at outlet glaciers, interpreted as a consequence of their different ice loss over the same period. A lower mean altitude of an outlet glacier typically results in a larger retreat and thus in more deformation around this glacier. Disturbances in LOS velocities are caused by glacial surges, subsidence at a volcanic center, and a magmatic intrusion. We used GIA modeling with the geometry of Vatnajökull ice cap, two horizontal Earth layers, and a prior ice model for the Icelandic ice caps to infer crustal and mantle rheology. The results indicate that InSAR and GPS are sensitive to different aspects of the Earth model. The combination of both, as seen in the probability distribution plots, provides good constraints on the elastic thickness and viscosity. Based on our assumptions, we found best-fit elastic thicknesses in the range of 15–40 km, and viscosities ranging from $4–10 \times 10^{18}$ Pa s, depending on the different data sets used.

Appendix A: Probability of a Model Given Observations

[30] Parameters of a model, **m**, are derived by fitting data (observations), **d**, to the predictions of a model function **G**(.) that maps the model parameters to the observations (entities in bold being vectors or matrices). Probability distributions for model parameters can be evaluated by a general statistical approach based on Baye's rule [*Hooper et al.*, 2012]. According to Bayes' rule,

$$p(\mathbf{m}|\mathbf{d}) = \frac{p(\mathbf{d}|\mathbf{m})p(\mathbf{m})}{\int_{-\infty}^{\infty} p(\mathbf{d}|\mathbf{m})p(\mathbf{m})d\mathbf{m}} \tag{A1}$$

where $p(\mathbf{m})$ is the prior probability of the model, $p(\mathbf{d}|\mathbf{m})$ is the probability distribution of the data given the model (the likelihood function), and $p(\mathbf{m}|\mathbf{d})$ is the posterior probability of the model given the data.

[31] Assuming the deviation of observations from their true values (errors) follows a multivariate Gaussian distribution, then

$$p(\mathbf{d}|\mathbf{m}) = \frac{1}{\sqrt{(2\pi)^n|\mathbf{Q}|}} \exp\left[-\frac{(\mathbf{d}-\mathbf{G}(\mathbf{m}))^{\mathrm{T}}\mathbf{Q}^{-1}(\mathbf{d}-\mathbf{G}(\mathbf{m}))}{2}\right] \tag{A2}$$

where **Q** is the variance-covariance matrix of the data and n is the number of observations.

[32] Assuming a uniform prior probability for data and model and considering equation (A2), the posterior probability is then

$$p(\mathbf{m}|\mathbf{d}) = K\frac{1}{\sqrt{(2\pi)^n|\mathbf{Q}|}} \exp\left[-\frac{(\mathbf{d}-\mathbf{G}(\mathbf{m}))^{\mathrm{T}}\mathbf{Q}^{-1}(\mathbf{d}-\mathbf{G}(\mathbf{m}))}{2}\right] \tag{A3}$$

where K is a constant defined by $p(\mathbf{m})/p(\mathbf{d})$.

Appendix B: Variance-Covariance Matrix Estimation of InSAR Observations

[33] The variance-covariance matrix for each of the InSAR tracks was evaluated as follows. We first deramped (i.e., removed the orbital and atmosphere ramps corresponding to parallel fringes across the scenes caused by incorrect orbital trajectories) the interferograms of the time series, because a ramp is estimated deterministically and does not contribute to the stochastic error. We then used the bootstrap method developed by *Efron and Tibshirani* [1993] on the deramped interferograms to derive the probability distribution of velocity estimates for each PS. We assumed that the covariance was a function of distance only and estimated this function by building an experimental variogram. We did this by selecting 500,000 random pairs of PS points and calculating the covariance for each pair. By binning the covariances for the 500,000 pairs based on their separation distance (lag), we were able to estimate an exponential covariance function (Figure B1). This function is defined by two parameters, the sill, corresponding to the zero lag covariance value, and the range describing how fast the exponential decays with

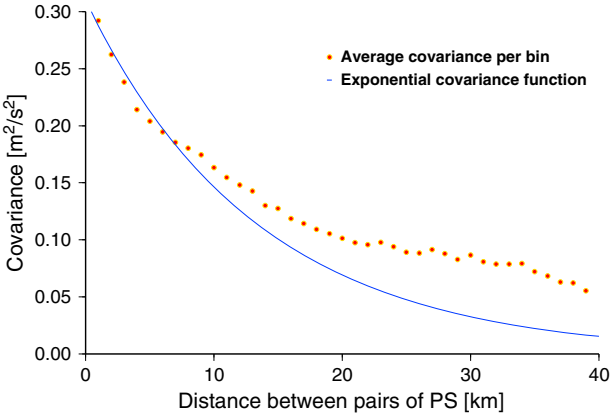

Figure B1. Plot showing the fitting of the exponential covariance function (blue line) to the average covariances binned as function of distance (red dots) for the ERS track 9. The sill and range are equal to 0.31 and 40,000, respectively.

distance. The covariance can only be reliably estimated for up to half the maximum distance in the scene, corresponding to ∼40 km in our InSAR tracks. We then built the variance-covariance matrix by applying this function to each pair of PS points in our results. For the diagonal terms of the variance-covariance matrix, we assumed a contribution from the exponential covariance function, plus an extra random noise term which is different for every observation. Therefore, we used the variance estimates directly from the bootstrapping, except if they were lower than the zero lag covariance, in which case we used the zero lag covariance.

[34] **Acknowledgments.** This study was funded by a Ph.D. grant to Amandine Auriac and support to Freysteinn Sigmundsson from the University of Iceland Research Fund, the Icelandic Research Fund (Volcano Anatomy Project). The study also received funding from the European Union Seventh Framework Programme under grant agreement 308377 (Project FUTUREVOLC). The authors thank ESA for providing the ERS-1, ERS-2 and Envisat data and two anonymous reviewers for their helpful comments and suggestions for the improvement of this paper. The figures were created using the GMT software package *Wessel and Smith* [1998].

References

Albino, F., V. Pinel, and F. Sigmundsson (2010), Influence of surface load variations on eruption likelihood: application to two Icelandic subglacial volcanoes, Grímsvötn and Katla, *Geophys. J. Int.*, *181*, 1510–1524, doi:10.1111/j.1365-246X.2010.04603.x.

Árnadóttir, T., B. Lund, W. Jiang, H. Geirsson, H. Björnsson, P. Einarsson, and T. Sigurdsson (2009), Glacial rebound and plate spreading: results from the first countrywide GPS observations in Iceland, *Geophys. J. Int.*, *177*, 691–716, doi:10.1111/j.1365-246X.2008.04059.x.

Barnhoorn, A., W. van der Wal, and M. R. Drury (2011), Upper mantle viscosity and lithospheric thickness under Iceland, *J. Geodyn.*, *52*, 260–270, doi:10.1016/j.jog.2011.01.002.

Björnsson, H. (1978), The surface area of glaciers in Iceland, *Jökull*, *28*, 31.

Björnsson, H., and F. Pálsson (2008), Icelandic glaciers, *Jökull*, *58*, 365–386.

Björnsson, H., F. Pálsson, and H. H. Haraldsson (2002), Mass balance of Vatnajökull (1991-2001) and Langjökull (1996-2001), Iceland, *Jökull*, *51*, 75–78.

Bowin, C., and J. Milligan (1985), Negative gravity anomaly over spreading rift valleys: Mid-Atlantic Ridge at 26°N, *Tectonophysics*, *113*, 233–256.

Cochran, J. R. (1979), An Analysis of Isostasy in the World's Oceans 2. Midocean Ridge Crests, *J. Geophys. Res.*, *84*, 4713–4729.

Darbyshire, F. A., I. T. Bjarnason, R. S. White, and O. G. Flóvenz (1998), Crustal structure above the Iceland mantle plume imaged by the ICEMELT refraction profile, *Geophys. J. Int.*, *135*, 1131–1149.

Efron, B., and R. J. Tibshirani (1993), An Introduction to the Bootstrap, Chapman & Hall, New York and London.

Einarsson, P., and K. Saemundsson (1987), Earthquake epicenters 1982-1985 and volcanic systems in Iceland (map), Í Hlutarsins Eli: Festschrift for Thorbjorn Sigurgeirsson.

Fleming, K., Z. Martinec, and D. Wolf (2007), Glacial-isostatic adjustment and the viscosity structure underlying the Vatnajökull Ice Cap, Iceland, *Pure Appl. Geophys.*, *164*, 751–768, doi:10.1007/s00024-007-0187-6.

Geirsson, H., *et al*., (2010), Overview of results from continuous GPS observations in Iceland from 1995 to 2010, *Jökull*, *60*, 3–22.

Grapenthin, R., F. Sigmundsson, H. Geirsson, T. Árnadóttir, and V. Pinel (2006), Icelandic rhytmics: annual modulation of land elevation and plate spreading by snow load, *Geophys. Res. Lett.*, *33*, doi:10.1029/2006GL028081.

Hooper, A. (2010), A Statistical-Cost Approach to Unwrapping the Phase of InSAR Time Series, *Proceedings FRINGE Workshop*, *Frascati*, *2009*.

Hooper, A., B. Ófeigsson, F. Sigmundsson, B. Lund, P. Einarsson, H. Geirsson, and E. Sturkell (2011), Increased capture of magma in the crust promoted by ice-cap retreat in Iceland, *Nat. Geosci.*, doi:10.1038/NGEO1269.

Hooper, A., J. Pietrzak, H. Simons, W. CUi, R. Riva, M. Naeije, A. Terwisscha van Scheltinga, E. Schrama, G. Stelling, and A. Socquet (2012), Importance of horizontal seafloor motion on tsunami height for the 2011 Mw=9.0 Tohoku-Oki earthquake, *Earth Planet. Sci. Lett.*, doi:10.1016/j.epsl.2012.11.013.

Hooper, A., P. Segall, and H. Zebker (2007), Persistent scatterer interferometric synthetic aperture radar for crustal deformation analysis, with application to Volcán Alcedo, Galápagos, *J. Geophys. Res.*, *112*, doi:10.1029/2006JB004763.

Jacoby, W. R., O. Hartmann, H. Wallner, P. L. Smilde, S. Bürger, L. E. Sjöberg, S. Erlingsson, D. Wolf, V. Klemann, and I. Sasgen (2009), Temporal gravity variations near shrinking Vatnajökull ice cap, Iceland, *Pure Appl. Geophys.*, *166*, 1283–1302, doi:10.1007/s00024-009-0499-9.

Kampes, B., and S. Usai (1999), Doris: the Delft Object-oriented Radar Interferometric Software, *2nd International Symposium on Operationalization of Remote Sensing*, *Enschede*, *The Netherlands*.

Klemann, V., and D. Wolf (2005), The eustatic reduction of shoreline diagrams: implications for the inference of relaxation-rate spectra and the viscosity stratification below Fennoscandia, *Geophys. J. Int.*, *162*, 249–256, doi:10.1111/j.1365-246X.2005.02637.x.

Larsen, C. F., R. J. Motyka, J. T. Freymueller, K. A. Echelmeyer, and E. R. Ivins (2005), Rapid viscoelastic uplift in southeast Alaska caused by post-Little Ice Age glacial retreat, *Earth Planet. Sci. Lett.*, *237*, 548–560, doi:10.1016/j.epsl.2005.06.032.

Milne, G. A., J. X. Mitrovica, H.-G. Scherneck, J. L. Davis, J. M. Johansson, H. Koivula, and M. Vermeer (2004), Continuous GPS measurements of postglacial adjustment in Fennoscandia: 2. Modeling results, *J. Geophys. Res.*, *109*, doi:10.1029/2003JB002619.

Norðahl, H., O. Ingólfsson, H. Pétursson, and M. Hallsdóttir (2008), Late Weichselian and Holocene environmental history of Iceland, *Jökull*, *58*, 343–364.

Pagli, C., and F. Sigmundsson (2008), Will present day glacier retreat increase volcanic activity? Stress induced by recent glacier retreat and its effect on magmatism at the Vatnajökull ice cap, Iceland, *Geophys. Res. Lett.*, *35*, doi:10.1029/2008GL033510.

Pagli, C., F. Sigmundsson, B. Lund, E. Sturkell, H. Geirsson, P. Einarsson, T. Árnadóttir, and S. Hreinsdóttir (2007), Glacio-isostatic deformation around the Vatnajökull ice cap, Iceland, induced by recent climate warming: GPS observations and finite element modeling, *J. Geophys. Res.*, *112*, doi:10.1029/2006JB004421.

Peltier, W. R. (2004), Global Glacial Isostasy and the Surface of the Ice-Age Earth: The ICE-5G (VM2) Model and GRACE, *Annu. Rev. Earth Planet. Sci.*, doi:10.1146/annurev.earth.32.082503.144359.

Rosen, P. A., S. Hensley, and G. Peltzer (2004), Updated Repeat Orbit Interferometry Package Released, *EOS Trans. AGU*, *85*(5), 47, doi:10.1029/2004EO050004.

Schmidt, P., B. Lund, and C. Hieronymus (2012a), Implementation of the glacial rebound pre-stress advection correction in general-purpose finite element analysis software: Springs versus foundations, *Comput. Geosci.*, *40*, 97–106, doi:10.1016/j.cageo.2011.07.017.

Schmidt, P., B. Lund, T. Árnadóttir, and H. Schmeling (2012b), Effects of dehydration stiffening in the mantle constrained by glacial rebound in Iceland, *Earth Planet. Sci. Lett.*, *359–360*, 152–161, doi:10.1016/j.epsl.2012.10.015.

Sigmundsson, F. (1991), Post-glacial rebound and asthenosphere viscosity in Iceland, *Geophys. Res. Lett.*, *18*(6), 1131–1134.

Sigmundsson, F., and P. Einarsson (1992), Glacio-isostatic crustal movements caused by historical volume change of the Vatnajökull ice cap, Iceland, *Geophys. Res. Lett.*, *19*(21), 2123–2126.

Sigmundsson, F., R. Pedersen, K. L. Feigl, V. Pinel, and H. Björnsson (2006), Elastic Earth response to glacial surges: Crustal deformation associated with rapid ice flow and mass redistribution at Icelandic outlet glaciers observed by InSAR, *Geophys. Res. Abstr.*, *8*, SRef-ID: 1607-7962/gra/EGU06-A-07822.

Sigmundsson, F., V. Pinel, B. Lund, F. Albino, C. Pagli, H. Geirsson, and E. Sturkell (2010), Climate effects on volcanism: influence on magmatic systems of loading and unloading from ice mass variations, with examples from Iceland, *Philosophical Transactions of the Royal Society*, *368* (1919), 2519–34, doi:10.1098/rsta.2010.0042.

Sjöberg, L. E., M. Pan, S. Erlingsson, E. Asenjo, and K. Arnason (2004), Land uplift near Vatnajökull, Iceland, as observed by GPS in 1992, 1996 and 1999, *Geophys. J. Int.*, *159*, 943–948, doi:10.1111/j.1365-246X.2004.02353.x.

Steffen, H., and G. Kaufmann (2005), Glacial isostatic adjustment of Scandinavia and northwestern Europe and the radial viscosity structure of the Earth's mantle, *Geophys. J. Int.*, *163*, 801–812, doi:10.1111/j.1365-246X.2005.02740.x.

Sturkell, E., F. Sigmundsson, and R. Slunga (2006), 1983-2003 decaying rate of deflation at Askja caldera: Pressure decrease in an extensive magma plumbing sustem at a spreading plate boundary, *Bull. Volcanol.*, *68*, 727–735, doi:10.1007/s00445-005-0046-1.

Wessel, P., and W. H. F. Smith (1998), New, improved version of generic mapping tools released, *Eos*, *Transactions American Geophysical Union*, *79*(47), 579–579, doi:10.1029/98EO00426.

Wolf, D., F. Barthelmes, and F. Sigmundsson (1997), Gravity, Geoil and Marine Geodesy, chap. Predictions of deformation and gravity change caused by recent melting of the Vatnajökull ice cap, Iceland, pp. 311–319, Springer-Verlag, Berlin.

Wu, P. (2004), Using commercial finite element packages for the study of earth deformations, sea levels and the state of stress, *Geophys. J. Int.*, *158*, 401–408, doi:10.1111/j.1365-246X.2004.02338.x.

Zebker, H. A., and J. Villasenor (1992), Decorrelation in Interferometric Radar Echoes, *IEEE Trans. Geosci. Remote Sens.*, *30*, 950–959.

de Zeeuw-van Dalfsen, E., R. Pedersen, A. J. Hooper, and F. Sigmundsson (2012), Subsidence of Askja caldera 2000-2009: Modelling of defor,ation processes at an extensional plate boundary, constrained by time series InSAR analysis, *J. Volcanol. Geotherm. Res.*, pp. 72–82, doi:10.1016/j.jvolgeores.2011.11.004.